Atomistic simulation of the influence of pre-existing stress on the interpretation of nanoindentation data

J. David Schall and Donald W. Brenner
Department of Materials Science and Engineering, North Carolina State University, Raleigh, North Carolina 27695

(Received 2 June 2004; accepted 9 June 2004)

By using molecular dynamics simulations, we have accurately determined the true contact area during plastic indentation of materials under an applied in-plane stress. We found that the mean pressure calculated from the true contact area varied slightly with applied pre-stress with higher values in compression than in tension and that the modulus calculated from the true contact area is essentially independent of the press-stress level in the substrate. These findings are largely consistent with the findings of Tsui, Pharr, and Oliver. On the other hand, if the contact area is estimated from approximate formulae, the contact area is underestimated and shows a strong dependence on the pre-stress level. When it is used to determine mean pressure and modulus, the empirically determined area leads to large errors. Our simulations demonstrate that this phenomenon, first reported for macroscale hardness measurements dating back to 1932, also exists at the nanometer-scale contact areas, apparently scaling over 10 orders of magnitude in contact area, from ~mm^2 to ~100 nm^2.

I. INTRODUCTION

In the past 20 years, nanoindentation has developed into a reliable means to measure mechanical properties, particularly at fine scales. Many examples of the utility of nanoindentation exist in the literature. For example, nanoindentation has been found to be useful in determining thin film properties where very shallow indentations are required.[1] With nanoindentation, point to point variations due to phase segregation, surface structures, and surface stress distributions may also be determined.[2–4] The test relies on the continuous monitoring of force and displacement as the indenter penetrates the sample.[5–8] The resulting force-displacement curves are used to determine the mechanical properties, most typically hardness and elastic modulus. A schematic diagram of a typical force-displacement curve is shown in Fig. 1. Hardness, which is normally defined as a mean pressure P_m, is given by

$$P_m = \frac{P_{\max}}{A} \quad , \tag{1}$$

where P_{max} is the maximum load or force during an indentation cycle and A is the projected area of the indentation at the maximum load. The reduced modulus E_r is given by

$$E_r = \frac{S}{2}\sqrt{\frac{\pi}{A}} \quad , \tag{2}$$

where S is the unloading stiffness or initial slope of the unloading curve and A again is the projected contact area at maximum load.[9] Although a value for S can be obtained easily from experimental force-displacement curves as indicated in Fig. 1, the projected area during indentation cannot be easily measured. Typically, either the dimensions of a remaining impression are measured optically after unloading, a finite element calculation is used to estimate contact area, or an empirical calculation is made. For the latter, the projected area of contact is typically estimated using an empirically determined shape function $A = f(h_p)$, where h_p is defined as the depth of plastic contact. Several methods with varying degrees of accuracy have been proposed. Field and Swain suggested a very crude model for spherical indenters based solely on geometrical considerations. To a first approximation, the depth of plastic contact h_p may be estimated as

$$h_p = \frac{h_t + h_r}{2} \quad , \tag{3}$$

where h_t is the maximum displacement and h_r is the depth of the residual impression after the load is removed.[10] We will refer to this approximation in the remainder of the paper as the Field and Swain (FS) method.

DOI: 10.1557/JMR.2004.0410

 © 2004 Materials Research Society

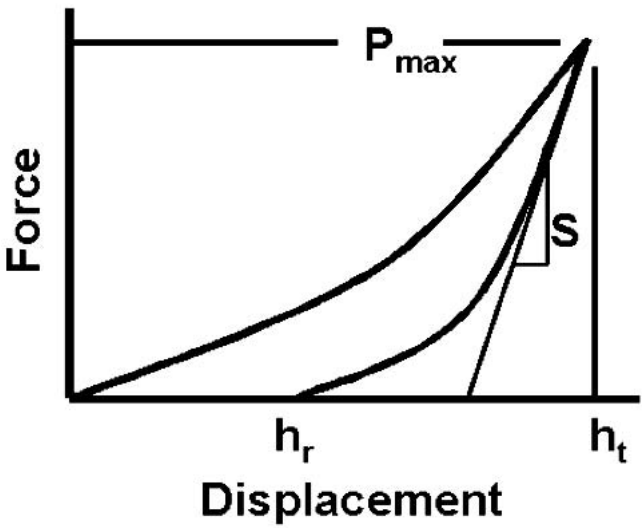

FIG. 1. Schematic representation of a force displacement curve for loading and unloading, indicating stiffness S as the slope of the unloading curve at peak load, total displacement h_t at peak load, and the residual deformation h_r after unloading.

In the case of a spherical indenter of radius R, the depth of plastic contact is then used to estimate the radius of contact a of the indenter

$$a = \sqrt{2Rh_p - h_p^2} \quad . \tag{4}$$

The projected contact area is given as $A = \pi a^2$. In 1992, Oliver and Pharr proposed a more robust approximation that accounts for the curvature of the unloading curve and provides a physically justifiable estimation for the depth of plastic contact.[9] In this classic model, the depth of plastic contact is given by

$$h_p = h_t - \epsilon \frac{P_{\max}}{S} \quad , \tag{5}$$

where again h_t is the maximum displacement, P_{max} is the maximum load, and S is the unloading stiffness. The constant ϵ is a geometrical factor related to the deflection of the surface at the contact perimeter that depends on the indenter geometry. For a shallow indentation with a spherical indenter, ϵ is equal to that of a parabola of revolution or 0.75. This approximation will be referred to as the OP method below. For a parabola of revolution or spherical indenter, h_p may be substituted into Eq. 4 to determine the radius of contact and thus the projected contact area A.

One example where the importance of accurate area determination is clearly illustrated is the effect of pre-stress in substrates on hardness and modulus measurements. Studies performed since the 1930s using a range of hardness measurement techniques have indicated a dependence of hardness on applied in-plane uni- and bi-axial strain, and as early as 1952 it was suggested that such changes could be used to measure residual surface stresses for metals.[11–15] In certain cases, increases in hardness under compressive in-plane strain and decreases in hardness of in-plane tensile strain were observed. To illustrate this trend at the macroscopic scale, Rockwell B hardness data of an annealed high-carbon steel from the 1952 Sines and Carlson study[12] has been redrawn in Fig. 2(a). The percent change in hardness relative to the unstressed state has been plotted as a function of relative in-plane stress. We have normalized the applied stress by the yield strength for annealed high carbon steel, which we approximated to be 350 MPa. (Sines and Carlson did not report the yield stress nor alloy composition for the material.) This results in a scale varying between −1 and 1 where a value of −1 corresponds to a compressive stress equal to that of the yield strength, 0 is the unstressed state, and 1 corresponds to a tensile stress equal to the yield strength. All hardness values have been normalized to the hardness at the unstressed state. Traditionally, this behavior had been attributed to the contribution of stresses from the in-plane strain and the local strain from the indentation to the resolved shear stress.[12,14] However like the FS and OP methods described above, the Rockwell hardness test is also empirical in nature. In the test, a known load is applied to the substrate through a steel ball. The depth of the plastic loading is estimated through the machinery of the tester and translated into a hardness number, that is, *the Rockwell hardness scale*. The accuracy of the test depends on careful calibration using materials of known hardness. In 1996, Tsui, Pharr, and Oliver (TPO) pointed out that changes in elastic modulus in pre-stressed substrates relative to the unstressed material appear too large to have physical significance, a result that called into question the interpretation of prior hardness data.[16] By indenting a polycrystalline aluminum alloy subjected to varying levels of a uniaxial strain, TPO showed that the slope of the unloading curve portion of the force-displacement curve at maximum load is independent of the strain level. TPO hypothesized that any apparent change in modulus (and hardness) with in-plane strain is primarily due to changes in contact area incorrectly produced by the empirical expressions. Through careful direct optical measurement of the contact impression, they determined that the true contact area was independent of the pre-stress state and thus the modulus is also independent of the pre-stress state. For comparison, we have redrawn the modulus data from TPO in Figs. 2(b) and 2(c). The modulus calculated using the empirically estimated contact area is shown in Fig. 2(b) and the modulus corrected using the true contact area is shown in Fig. 2(c). The pre-stress has been normalized by the reported yield strength for the Al alloy used in the TPO experiment (353.1 MPa). The error in the empirical estimates has been shown in experiment and finite element

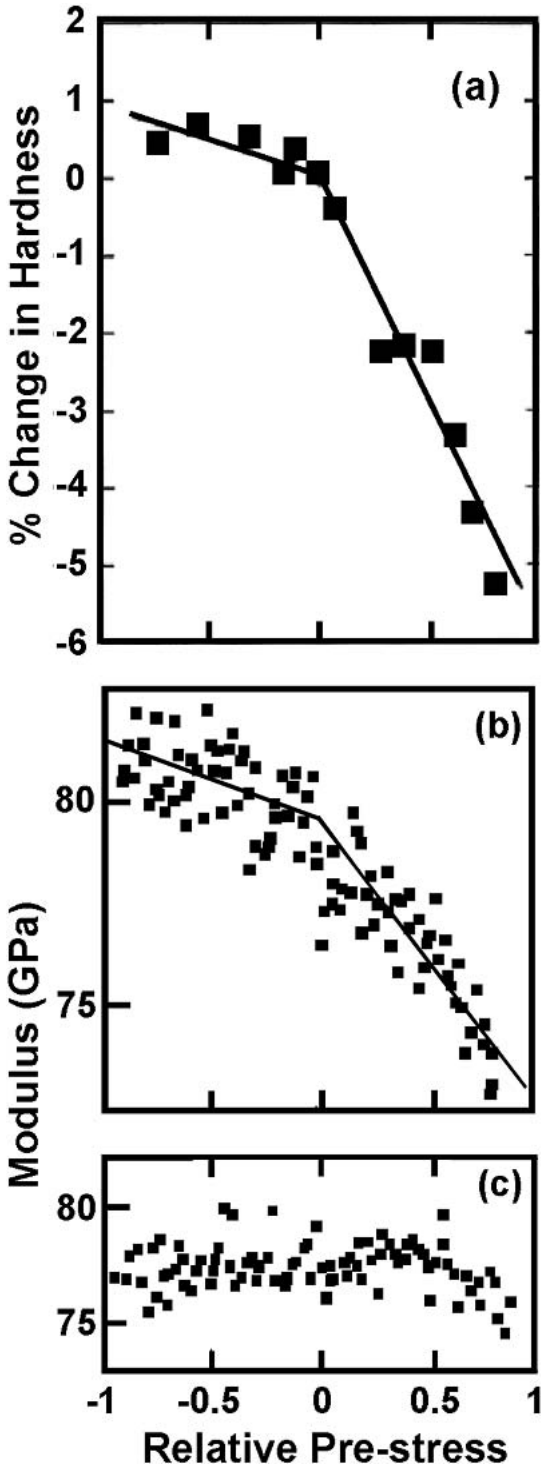

FIG. 2. (a) Sines and Carlson hardness data as a function of relative pre-stress. The percent change in hardness is relative to the hardness at zero pre-stress. Pre-stress is relative to an estimated yield stress of 350 MPa. Negative values denote compression, positive values denote tension. (b) TPO data for modulus redrawn from Ref. 16 as a function of pre-stress calculated using the Oliver-Pharr estimate for the contact area. (c) TPO data for modulus redrawn from Ref. 16 as a function of relative pre-stress calculated using the optically measured estimate for the contact area. Pre-stress in (b) and (c) relative to the yield stress reported in Ref. 16.

simulations to be due to material pileup around the indenter.[17] This error is largely minimized in hard materials where pileup is not present. In further studies using finite element calculations, Chen and Vlassak found that in some cases for soft materials that the contact area may be underestimated using the empirical expressions by as much as 66%.[18]

As illustrated by this example, the accuracy of the projected contact area approximation or measurement may greatly affect the interpretation of indentation results. The TPO nanoindentation experiments were conducted using a Berkovich diamond indenter which left contact impressions on the order 100 μm^2. Earlier experimental studies that reported a change in hardness with in-plane stress had much larger contact areas, up to mm^2. In this paper, we revisit the issue of the effect of pre-stress on the modulus and hardness, but on a much smaller scale (that of about a 100 nm^2 contact area) in single crystal gold, a soft material that shows significant pileup after a plastic indentation. This scale of contact area is rapidly becoming the realm of features relevant to the electronics industry. We will use molecular dynamics simulations of spherical indentation to compare and contrast the empirical FS and OP area estimates with direct contact area measurement for substrates across a range of pre-existing stresses. The empirically determined areas lead to the same faux change in modulus and hardness as have been found previously. As was shown by the TPO experiments, when direct measurement of contact area is made, changes in modulus are not apparent except at the highest tensile strains. These results, together with prior finite element modeling and experimental studies over a wide range of indentation scales, show that this effect *is remarkably independent of the scale of contact*.

II. METHOD

The molecular dynamics code *Paradyn* developed by Plimpton[19] was used to model the indentation of (111) oriented gold surfaces. *Paradyn* uses embedded-atom method potentials such as those developed by Foiles, Daw, and Baskes to model atomistic behavior of face-centered-cubic (fcc) and other close-packed metals.[20,21] For such materials, the embedded atom formalism has proven to be particularly good at modeling bulk and defect properties such as energies and structures and has been used extensively to model the onset of plasticity during the nanoindentation of gold in quasi-static (0 temperature) simulations of nanoindentation and to a smaller extent molecular dynamics studies of indentation.[22–25] The materials constants derived from the Au potential used in this study are given in Table I.[21]

TABLE I. Materials properties of gold derived from the embedded atom potential as reported by Foiles, Daw, and Baskes in Ref. 21.

a_o	4.08
B	1.67 erg/cm^3
E_{coh}	3.93 eV
E_v^f	1.03 eV
C_{11}	1.83 erg/cm^3
C_{12}	1.59 erg/cm^3
C_{44}	0.45 erg/cm^3

Equilibrium lattice constant (a_o), bulk modulus (B), cohesive energy (E_{coh}), vacancy formation energy (E_v^f), and elastic constants (C_{11}, C_{12}, C_{44}).

The indenter-substrate interactions were modeled using a purely repulsive potential form. The force from the indenter I on substrate atom i is given as

$$F_i = 0 \text{ for } r_{iI} \geqslant R$$
$$F_i = -k(R - r_{iI})^n \text{ for } r_{iI} < R \quad , \qquad (6)$$

where R defines the radius of a "virtual" spherical indenter, r_{iI} is the radial distance from the center of the indenter to atom i, and n and k are constants related to the stiffness of the indenter. A strictly repulsive interaction, which is similar to other recent simulations,[22–25] is intended to mimic nonadhesive contact. To simulate loading or unloading of the indenter, the coordinates defining the center of the sphere are changed incrementally such that the indenter is moved up or down in the direction normal to the substrate surface. The force on the indenter is calculated by summing the forces normal to the surface for all atoms in contact with the indenter ($r_{iI} < R$). The force data along with the displacement of the indenter are used to generate force-displacement curves. To obtain a measure of the true contact area in the simulations, the positions of atoms in contact with the virtual indenter are used to describe the geometry of the indenter/substrate contact. The area of the polygon inscribed by the atoms around the perimeter of the contact impression is taken to be the projected area. This is referred to below as the inscribed polygon (IP) method.

A schematic diagram of the model used in the simulated indentation tests is shown in Fig. 3. In the figure, the z-axis is taken to be the normal to the (111) plane, the x-axis is taken to be along the $[\bar{1}10]$ close-packed direction, and the y-axis forms a right-handed coordinate system along the $[\bar{1}\bar{1}2]$ direction. The bottom layer of atoms is held rigid in the z-direction, and the sides are maintained through periodic boundaries in the x and y directions.

In our simulations, we have chosen to simulate the entire indentation cycle using molecular dynamics. Due to the computational limitations inherent in molecular dynamics simulations, namely that of time-scale, the trade-off of this choice is that it requires a high indentation rate. The particles in each simulation are held at the thermal equivalent of 300 K via the generalized Langevin equation thermostat.[26] For each indentation simulation reported below, a molecular dynamics time step of 0.005 ps was used. At each time step the indenter was moved 0.01 Å down or up for loading or unloading. This results in an indentation rate of 2 Å/ps. Although much faster than experimental indentation rates, which are on the order of Å/s, the indentation rate in our simulations is still approximately eight times slower than the theoretical dislocation velocity in bulk gold. As a result the underlying plastic deformation mechanisms are largely independent of the indentation rate with the benefit that any thermally activated processes present in a typical indentation experiment may be accurately represented.

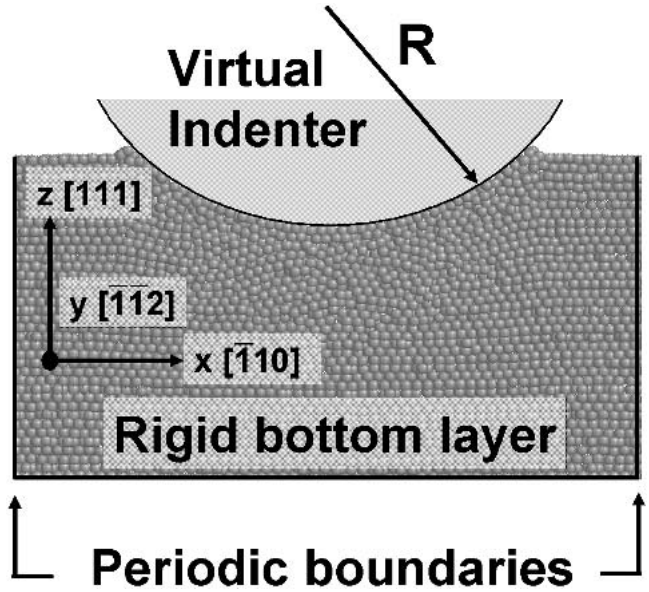

FIG. 3. Schematic diagram of the setup for the molecular dynamics simulation. The x axis is along the $[\bar{1}10]$ direction, y along a $[\bar{1}\bar{1}2]$ direction (normal to the plane of the illustration), and the z axis is oriented in the [111] direction. Periodic boundaries are held in the x and y directions. The bottom layer of atoms is held rigid. R is the radius of the virtual indenter.

Lilleodden et al.[24,25] have spent considerable effort in understanding indenter stiffness on the "virtual" indenter function expressed by Eq. (6). In their work they settled on values of n and k to be 2 and 10 eV/Å^3, respectively. Lilleodden uses a conjugate gradient energy minimization scheme to determine the equilibrium structure at each indentation displacement before moving to the next. This is equivalent to indenting at a very slow indentation rate but at zero temperature. Molecular dynamics simulations were performed only at specific points along the force-displacement curve where dislocation emission occurred as indicated by discontinuities in the force-displacement curves.

III. TESTING THE INDENTER

We conducted several test cases to qualify the indenter function. The results are significantly different than those

reported by Lilleodden and others for simulations using conjugate gradient minimization schemes and led us to the selection of different values for the indenter stiffness parameters n and k. Illustrated in Fig. 4(a) are the force-displacement curves of several small scale molecular dynamics simulations of indentation with varying values of the constant k at a constant value $n = 1$. A 10 Å radius indenter was used to indent a (111) oriented substrate with dimensions 70 Å × 70 Å × 70 Å to a depth of 5 Å at a constant displacement rate of 2 Å/ps. Small values of k (>0.5 eV/Å^2) suggest an overly compliant indenter which leads to little or no plastic deformation of the substrate. Large values of k (>5 eV/Å^2) cause bouncing of the atoms as they make and lose contact with the tip. This leads to noisy data making analysis of the force-displacement curves difficult. Shown in Fig. 4(b) are force-displacement curves of the same substrate with varying values for the exponent n with a constant of $k = 1$ eV/Å^{n+1}. Over the range of n evaluated no particular value appears to be better than another. Based on these tests we have found suitable values of n and k to be 1.0 and 1.0 eV/Å^2, respectively. For the range of indenter stiffness parameters tested it does not appear possible to back calculate a value for the modulus or Poisson's ratio of the indenter, a problem also noted by Lilleodden.[25] Therefore all modulus values reported below are for reduced modulus instead of the substrate modulus.

Finite element simulations by several other groups have reported observable periodic boundary effects for substrate thicknesses less than 50 times the indentation depth.[17,27] To determine the effect of the rigid boundary layer on indentation results in our simulations, three substrates with thicknesses of 6.3, 12.6, and 19 nm were indented to a maximum depth of 2 nm with a 10 nm radius indenter. The x and y dimensions were maintained at 30 nm and 30 nm for each substrate indented. The simulated force-displacement curves are shown in Fig. 5. Only minor differences were observed. The force-displacement curves for the 19- and 12.6-nm-thick substrates overlap completely, whereas the 6.3-nm-thick substrate shows only a slight increase in the force with displacement over the 19- and 12.6-nm substrates. This translates into an increase in hardness of only 2% and a negligible change in the reduced modulus. These results are consistent with the finite element simulations of soft thin-films on hard substrates conducted by Chen and Vlassak.[18] They observed that film thickness effects only have significant importance for indent depths greater than 50% of the film thickness. Our current computational resources limit us to simulations consisting of roughly one million atoms which corresponds to the substrate size of approximately 30 nm × 30 nm × 19 nm. The indentation depth was limited to 2 nm or approximately 10% of the total thickness of the substrate. Additional analysis of atomic stresses during indentation showed that the in-plane periodic boundary conditions do not influence the results significantly.

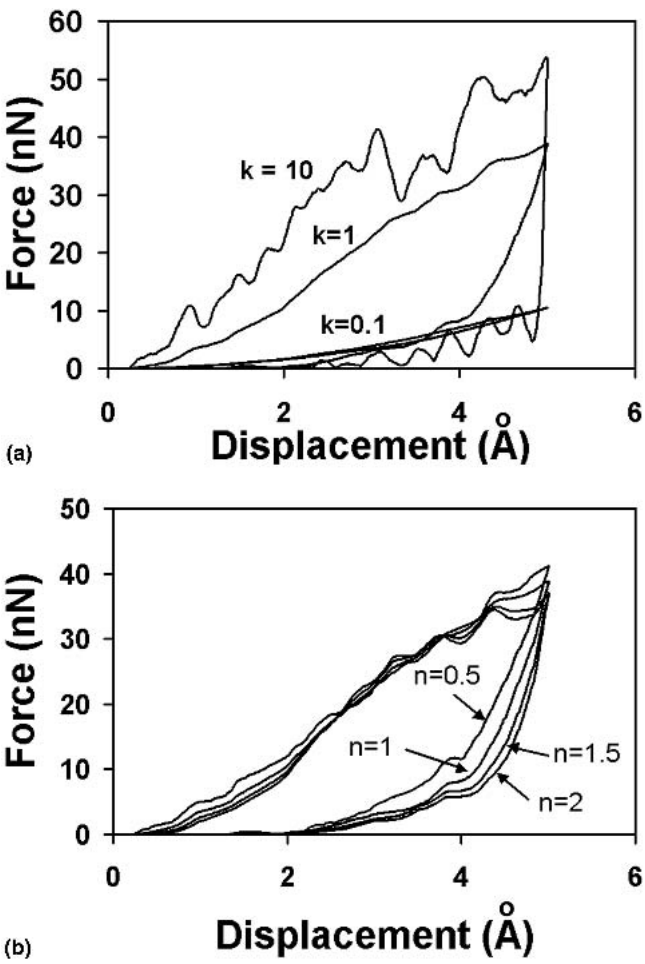

FIG. 4. Force-displacement curves for (a) varying values of the constant k with $n = 1$, and (b) for varying values of the constant n with $k = 1$.

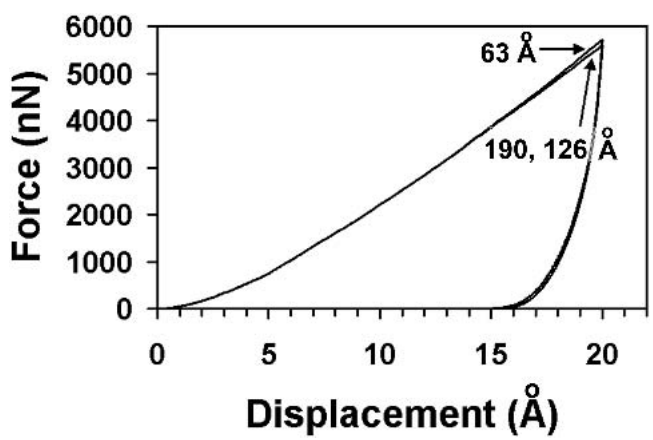

FIG. 5. Force-displacement curves for substrate thicknesses of 6.3, 12.6, and 19 nm indented to a depth of 2 nm with a 10-nm-radius indenter. The curves overlap completely for the 12.6- and 19-nm-thick substrates with only a slight increase in the force with displacement for the 6.3-nm substrate with respect to the other substrates.

To study the effect of method of projected area determination on calculation of modulus and hardness, a series of simulated nanoindentation experiments were conducted on substrates with pre-applied biaxial strains ranging between ±1.5%, where positive values indicate tension and negative values indicate compression. The substrates consist of 960,000 atoms with unstrained dimensions of approximately 30 nm × 30 nm × 19 nm. Strain was applied uniformly over the entire half-space in the in-plane x and y directions by multiplying each atomic coordinate by a strain factor $(1 + \epsilon)$ in the x direction and $(1 + \sqrt{3/2}\epsilon)$ in the y direction where ϵ is the applied strain. The factor of $\sqrt{3/2}$ ensures that the symmetry of the (111) plane is maintained. To maintain strain, the periodic boundary lengths in the x and y directions were also multiplied by their respective strain factors. The energy of the substrate was then minimized via a conjugate gradient step to achieve the correct contraction or expansion in the z direction. After minimization, the substrate was heated to 300 K and allowed to equilibrate. Each substrate was then indented with a 10-nm-radius indenter to a maximum load of approximately 4700 nN, which resulted in penetration depths between 1.6 nm for a strain of −1.5% and 1.9 nm for a 1.5% strain.

IV. RESULTS AND DISCUSSION

Permanent deformation was present upon unloading indicating the presence of plastic damage even though no discontinuities or pop-in events were observed in the force-displacement curves (Fig. 6). Interestingly, the true contact area in our simulations (as determined by the IP method) changes continuously with depth throughout the indentation cycle as illustrated in Fig. 7(a). The contact impression is fairly circular, and its perimeter only marginally reflects the underlying crystal symmetry as illustrated by the contact impression shown in Fig. 7(b). This behavior is significantly different from the discrete steps in the contact area as a function of depth and clear reflection of crystal symmetry observed for simulations where a conjugate gradient minimization methods were used.[24,25] We attribute these differences to the random thermal motion of atoms present in our simulations that are not present when conjugate gradient methods are used.

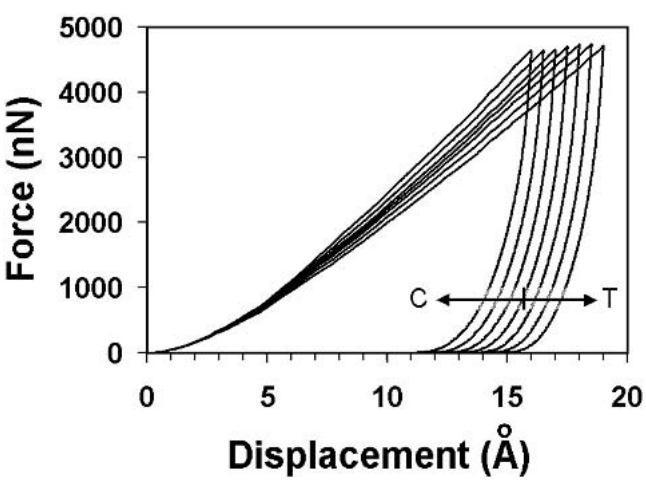

FIG. 6. Force-displacement curves for substrates with different levels of an applied pre-stress. Each substrate was loaded to approximately 4700 nN. C denotes loading curves under compressive pre-strain up to −1.5%. T denotes substrates under tensile pre-strain up to 1.5%.

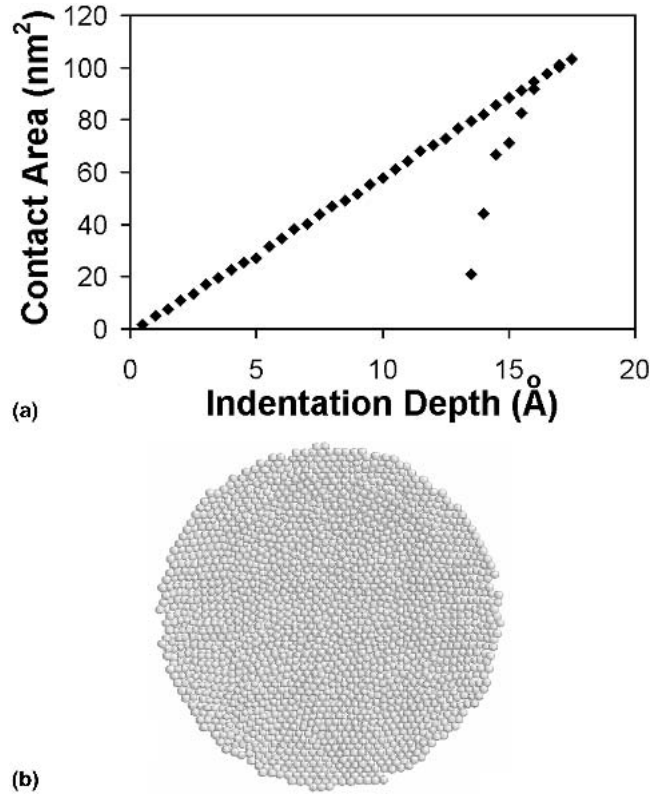

FIG. 7. (a) True contact area as measured by the inscribed polygon method as a function of indenter displacement for loading and unloading of the unstressed sample, and (b) the disk atoms in contact with the indenter at maximum load for the unstressed sample. The diameter of the disk is roughly 12 nm.

We begin our analysis by determining the projected contact area for each indentation. As suggested above, the true contact area may be determined in situ using the IP method, as the atomic coordinates of the perimeter of contact may be determined at any time step during the simulation. The projected contact area calculated using the FS approximation may be determined directly from the unloading curve. Determining the projected contact area using the OP method first requires that the unloading stiffness at the peak load be determined. The unloading stiffness was calculated by a linear least squares fit to the first ten data points of the unloading curve. Shown in Fig. 8 is the unloading stiffness plotted as a function of

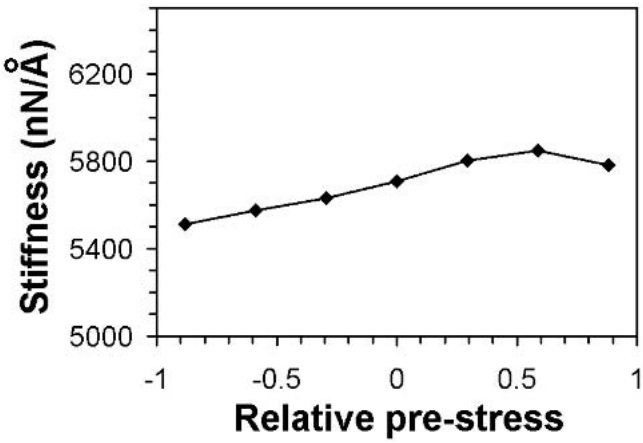

FIG. 8. The unloading stiffness as a plotted as a function of the relative pre-stress.

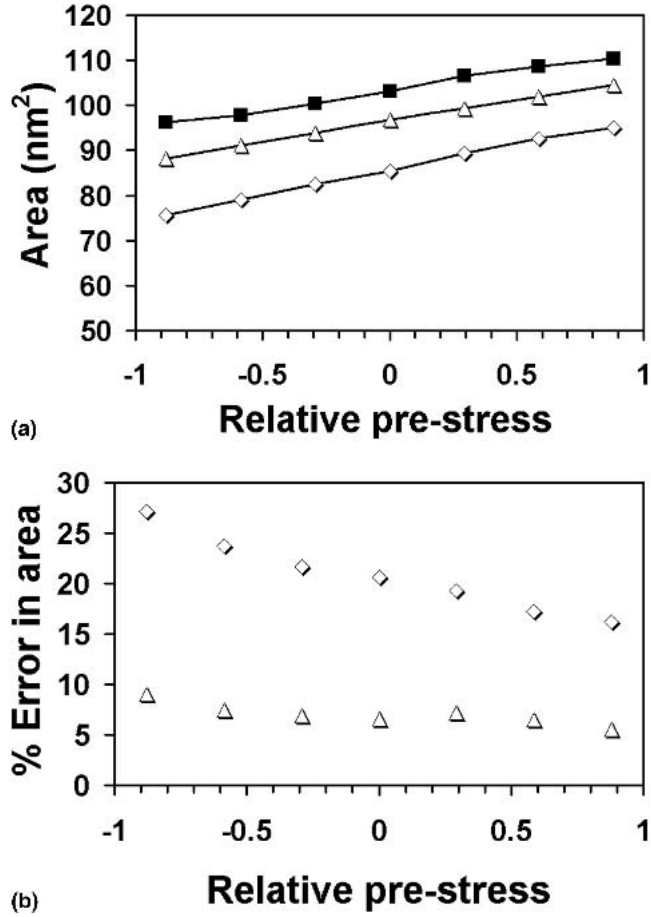

FIG. 9. (a) The projected contact area as function of the relative pre-stress for true area (filled squares), OP area (open triangles), and FS area (open diamonds) and (b) the percent error in the area estimation with respect to the true contact area for the OP method (open triangles) and FS method (open diamonds) as a function of the relative pre-stress.

relative pre-stress. Contrary to the experiments of TPO, the unloading stiffness is not independent of the pre-stress level. In Fig. 8 and subsequent figures, the pre-stress was calculated from the applied biaxial pre-strain using Hooke's law. For comparison to the experimental data of Sines and Carlson and TPO data in Fig. 2, each pre-stress level was then normalized by the yield strength. Again, this gives a scale varying between −1 and 1 where a value of −1 corresponds to a compressive stress equal to that of the yield strength, 0 is the unstressed state, and 1 corresponds to a tensile stress equal yield strength. Because the material is single crystal and is initially defect and dislocation free, we have assumed that the yield stress is equal to the theoretical yield strength of gold. This value was determined using the Frenkel[28] approximation through the expression $\tau_{th} = Gb/a2\pi$, where G is the shear modulus, b is the distance between atoms in the slip direction, and a is the distance between slip planes. The projected contact areas as determined using all three methods have been plotted as a function of the relative pre-stress in Fig. 9(a). The FS areas are indicated by open diamonds, the OP areas are indicated by open triangles, and the true IP areas are represented by filled squares. The percent error of the FS (open diamonds) and OP (open triangles) estimated areas relative to the true (IP) contact area is shown in Fig. 9(b). The error is not consistent across the range of the pre-stress, and the amount of error tends to be higher in compression than in tension. This will cause errors in not only the relative values of the hardness and modulus but also the dependence in the hardness and modulus with the applied pre-stress. At the highest level of compressive pre-stress, the FS method underestimates the contact area by as much as 27%. The OP method is somewhat better with a maximum underestimation of area in compression of 9%. The lowest values of error appear in tension and are 16% and 5% for the FS and OP methods, respectively. It should also be noted that the true contact area as calculated by the IP method is not independent of the pre-stress level, contrary to the results of the TPO experiments. To illustrate the extent of the errors caused by the empirical formulas, we have plotted the mean pressure and reduced modulus using each method of area determination in Figs. 10(a) and 11(a). The percent change in mean pressure and modulus relative to the zero pre-stress state has been plotted in Figs. 10(b) and 11(b). In both Figs. 10 and 11, the open diamonds represent the mean pressure or reduced modulus determined using the FS model, open triangles represent the mean pressure or modulus determined using the OP method, and the filled squares represent the mean pressure or modulus determined using the true area from the IP method. As illustrated in Fig. 10(a), the FS method causes a large overestimation in the mean pressure with the largest overestimation in compression. The OP method overestimates the mean pressure but to a much smaller extent. In our simulations, the mean pressure is not constant across all

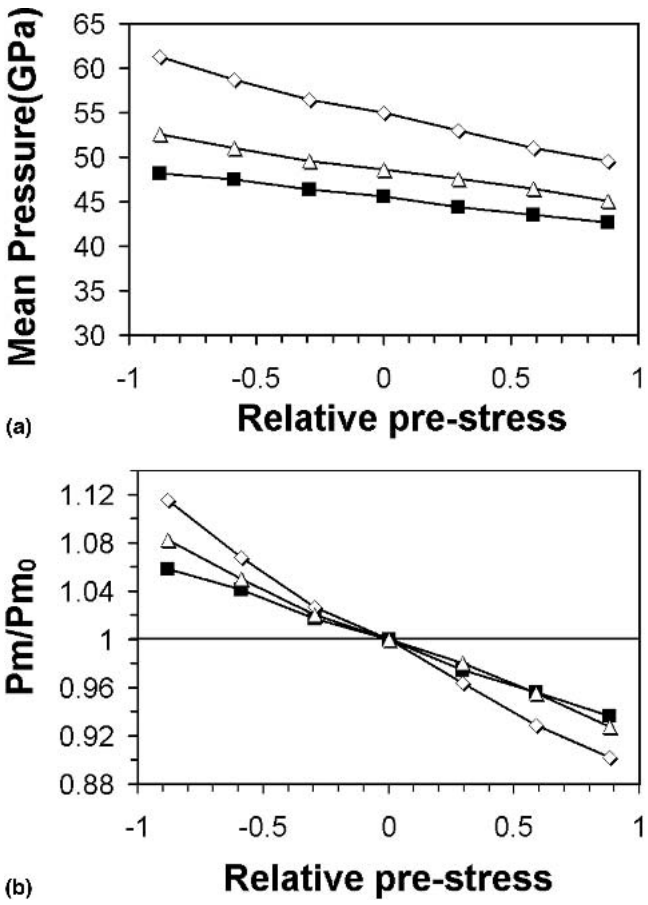

FIG. 10. (a) Mean pressure as a function of relative pre-stress as calculated using the true area (filled squares), OP method (open triangles), and FS method (open diamonds), and (b) the relative mean pressure with respect to the mean pressure at zero pre-stress for the true area (filled squares), OP method (open triangles), and FS method (open diamonds).

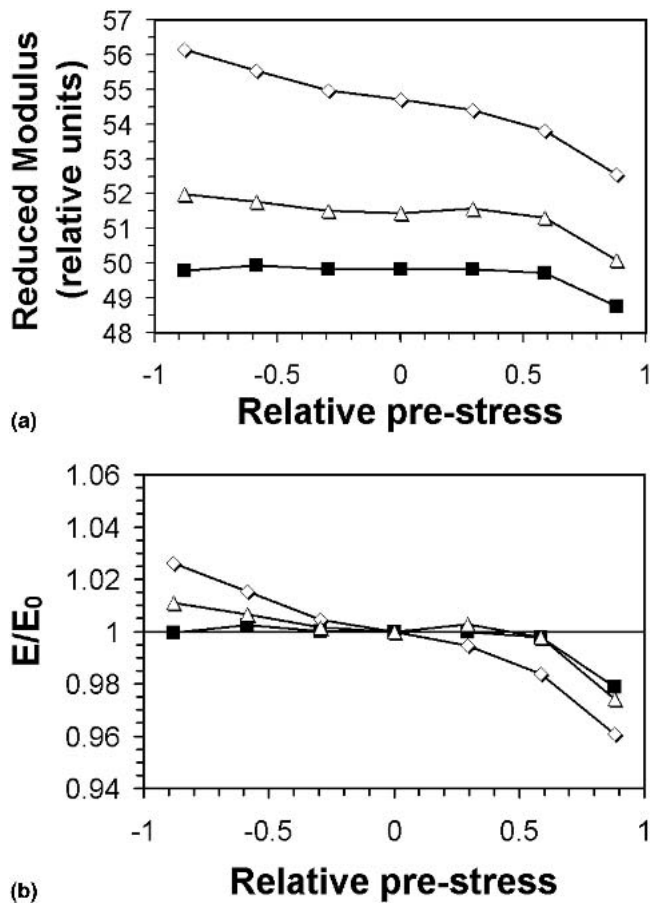

FIG. 11. (a) Reduced modulus as a function of relative pre-stress as calculated using the true area (filled squares), OP method (open triangles), and FS method (open diamonds), and (b) the relative reduced modulus with respect to the reduced modulus at zero pre-stress for the true area (filled squares), OP method (open triangles), and FS method (open diamonds).

levels of pre-stress even when the true contact area is used since the true contact area is not independent of the pre-stress level. As illustrated by Fig. 10(b), the OP method appears to model this trend very well except at the highest compressive pre-stress level, whereas the FS model tends to exaggerate the trend to a large degree. The same general results are observed in the modulus calculations shown in Fig. 11(a). Again, the FS model greatly overestimates the modulus, whereas the OP method provides a better but still high estimate. Despite the fact that we observe a dependence of both the true contact area and the unloading stiffness on the pre-stress level, the ratio of the stiffness to the square root of the true contact area appears to be independent of the pre-stress level. When used in the modulus calculation little or no change relative to the unstressed state is observed except at the highest tensile pre-stress level, a trend that was also observed by Tsui, Pharr, and Oliver [compare to Fig. 2(c)]. The OP method does a good job estimating the dependence (or lack of) of the modulus on the pre-stress level except at the highest compressive pre-stress level, as seen in Fig. 11(b), while the FS model suggests a false dependence of modulus on the pre-stress level similar to the data shown in Figs. 2(a) and 2(b).

V. CONCLUSION

We have illustrated through the use of molecular dynamics simulations the importance of accuracy in the calculation or measurement of the projected contact area on the interpretation of nanoidentation results. Based on these results, it appears that although the OP method underestimates the projected contact area and thus overestimates the mean pressure and modulus, it does a fairly good job for the system we have modeled at predicting the dependence of pre-stress on the mean pressure and modulus except at very high levels of the pre-stress. However, it should be noted that the same method failed to predict the correct results in the experiments of Tsui, Pharr, and Oliver. We show that simpler empirical area

estimations fail miserably to predict even the correct dependencies. We have also shown by way of comparison of these simulations to experiments in published literature that the determining the correct value contact area is important to the correct interpretation of indentations results at scales from square nanometers to square millimeters. A certain wariness of empirical estimates for contact areas and properties derived from them is advised when interpreting the results of new experiments or those published in the past. However, when the true contact area is used, values for mean pressure and modulus may be relied upon.

ACKNOWLEDGMENTS

This work was funded by the National Science Foundation through contract no. DMR-9971429. J.D.S. was also supported by the Southeast Universities Research Association as a summer research fellow at Oak Ridge National Laboratory. Insightful discussions with Phil Russell, Konrad Jarausch, J.J. Houston, Ron Scattergood, and George Pharr are gratefully acknowledged.

REFERENCES

1. M.F. Doerner and W.D. Nix: A method for interpreting the data from depth-sensing indentation instruments. *J. Mater. Res.* **1,** 601 (1986).
2. O.A. Shenderova, J.P. Mewkill, and D.W. Brenner: Nanoindentation as a probe of nanoscale residual stress. *Atomistic Simulation Results. Molecular Simulation* **25,** 81 (2000).
3. K.F. Jarausch, J.D. Kiely, J.E. Houston, and P.E. Russell: Defect-dependent elasticity: Nanoindentation as a probe of stress state. *J. Mater. Res.* **15,** 1693 (2000).
4. J.J. Gilman: In *The Science of Hardness Testing and Its Research Applications*, edited by J.H. Westbrook and H. Conrad (American Society for Metals, Metals Park, OH, 1973), pp. 51–74.
5. J.B. Pethica: In *Ion Implantation into Metals*, edited by V. Asheworth, W. Grant, and R. Procter (Pergamon Press, Oxford, U.K., 1982), pp. 147–156.
6. J.L. Loubet, J.M. Georges, O. Marchesini, and G. Meille: Vickers indentation curves of magnesium oxide (MgO). *J. Tribology* **106,** 43 (1984).
7. D. Newey, M.A. Wilkins, and H.M. Pollock: An ultra-low-load penetration hardness tester. *J. Phys. E: Sci. Instrum.* **15,** 119 (1982).
8. D. Stone, W.R. LaFontaine, P. Alexopoulos, T-W. Wu, and Che-Yu Li: An investigation of hardness and adhesion of sputter-deposited aluminum on silicon by utilizing acontinuous indentation test. *J. Mater. Res.* **3,** 141 (1988).
9. W.C. Oliver and G.M. Pharr: An improved technique for determining hardness and elastic modulus using load and displacement sensing indentation experiments. *J. Mater. Res.* **7,** 1564 (1992).
10. J.S. Field and M.V. Swain: A simple predictive model for spherical indentation. *J. Mater. Res.* **8,** 297 (1993).
11. S. Kokubo: *Science Reports of the Tohoku Imperial University.* **21,** 256 (1932).
12. G. Sines and R. Carlson: Hardness measurements for determination of residual stresses. *ASTM Bulletin* **180,** 35 (1952).
13. G.U. Oppel amd P.W. Hill: Strain measurements of the Root of Cracks and Notches, Proceeding of the Society for Experimental Stress Analysis **21,** 206 (1964).
14. T.R. Simes, S.G. Mellor, and D.A. Hills: A note on the influence of residual-stress on measured hardness. *J. Strain Analysis* **19,** 135 (1984).
15. W.R. LaFontaine: C.A. Paszkiet M.A. Korhonen, and Che-Yu Li: Residual stress measurements of thin aluminum metallizations by continuous indentation and x-ray stress measurement techniques. *J. Mater. Res.* **6,** 2084 (1991).
16. T.Y. Tsui, W.C. Oliver, and G.M. Pharr: Influences of stress on the measurement of mechanical properties using nanoindentation: Part I. Experimental studies in an aluminum alloy. *J. Mater. Res.* **11,** 752 (1996).
17. A. Bolshakov, W.C. Oliver, and G.M. Pharr: Influences of stress on the measurement of mechanical properties using nanoindentation: Part II. Finite element simulations. *J. Mater. Res.* **11,** 760 (1996).
18. X. Chen and J.J. Vlassak: Numerical study on the measurement of thin film mechanical properties by means of nanoindentation. *J. Mater. Res.* **16,** 2974 (2001).
19. S.J. Plimpton and B.A. Hendrickson: Parallel molecular dynamics with the embedded atom method, in *Materials Theory and Modelling,* edited by J. Broughton, P. Bristowe, and J. Newsam (Mater. Res. Soc. Symp. Proc. **291,** Pittsburgh, PA, 1993), p. 37.
20. M.S. Daw and M.I. Baskes: Embedded atom method: Derivation and application to impurities, surfaces, and other defects in metals. *Phys. Rev. B* **29,** 6443 (1984).
21. S.M. Foiles, M.I. Baskes, and M.S. Daw: Embedded atom method functions for the FCC metals Cu, Ag, Au, Ni, Pd, Pt and their alloys. *Phys. Rev. B* **33,** 7983 (1986).
22. C.L. Kelchner, S.J. Plimpton, and J.C. Hamilton: Dislocation nucleation and defect structure during surface indentation. *Phys. Rev. B* **58,** 11085 (1998).
23. J.A. Zimmerman, C.L. Kelchner, P.A. Klein, J.C. Hamilton, and S.M. Foiles: Surface step effects on nanoindentation. *Phys. Rev. Lett.* **87,** 165507 (2001).
24. E.T. Lilleodden, J.A. Zimmerman, S.M. Foiles, and W.D. Nix: Atomistic simulation of elastic deformation and dislocation nucleation during nanoindentation, *J. Mech. and Phys. Solids* **51,** 901 (2003).
25. E.T. Lilleodden: In *Indentation induced plasticity of thin metal films*. Ph.D. Thesis, Department of Materials Science and Engineering, Stanford University, Stanford, California, 2001.
26. R. Kubo: Fluctuation-dissipation theorem. *Rep. Prog. Theor. Phys.* **33,** 425 (1965).
27. G.M. Pharr and A. Bolshakov: Understanding nanoindentation unloading curves. *J. Mater. Res.* **17,** 2660 (2002).
28. J. Frenkel: *Z. Phys.* **37,** 572 (1926).